Automated *In Situ* Optimization and Disorder Mitigation in a Quantum Device

Jacob Benestad,[1,*] Torbjørn Rasmussen,[2,3,*] Bertram Brovang,[2,*] Oswin Krause,[4] Saeed Fallahi,[5,6] Geoffrey C. Gardner,[6] Michael J. Manfra,[5,6,7,8] Charles M. Marcus,[2] Jeroen Danon,[1] Ferdinand Kuemmeth,[2,9] Anasua Chatterjee,[2,3,†] and Evert van Nieuwenburg[10,‡]

[1]*Center for Quantum Spintronics, Department of Physics, Norwegian University of Science and Technology, NO-7491 Trondheim, Norway*

[2]*Center for Quantum Devices, Niels Bohr Institute, University of Copenhagen, 2100 Copenhagen, Denmark*

[3]*QuTech and Kavli Institute of Nanoscience, Delft University of Technology, 2600 GA Delft, The Netherlands*

[4]*Department of Computer Science, University of Copenhagen, 2100 Copenhagen, Denmark*

[5]*Department of Physics and Astronomy, Purdue University, West Lafayette, Indiana 47907, USA*

[6]*Birck Nanotechnology Center, Purdue University, West Lafayette, Indiana 47907, USA*

[7]*Elmore Family School of Electrical and Computer Engineering, Purdue University, West Lafayette, Indiana 47907, USA*

[8]*School of Materials Engineering, Purdue University, West Lafayette, Indiana 47907, USA*

[9]*Institute of Experimental and Applied Physics, University of Regensburg, 93040 Regensburg, Germany*

[10]*$\langle aQa^L\rangle$ at Lorentz Institute and Leiden Institute of Advanced Computer Science, Leiden University, P.O. Box 9506, 2300 RA Leiden, The Netherlands*

(Received 19 December 2024; revised 8 May 2025; accepted 20 October 2025; published 19 November 2025)

We investigate automated *in situ* optimization of the potential landscape in a quantum point contact device, using a 3×3 gate array patterned atop the constriction. Optimization is performed using the covariance matrix adaptation evolutionary strategy, for which we introduce a metric for how "steplike" the conductance is as the channel becomes constricted. We first perform the optimization of the gate voltages in a tight-binding simulation and show how such *in situ* tuning can be used to mitigate a random disorder potential. The optimization is then performed in a physical device in experiment, where we also observe a marked improvement in the quantization of the conductance resulting from the optimization procedure.

DOI: 10.1103/13c4-p4fq

Introduction—Machine learning has garnered increasing attention within quantum and condensed matter physics in recent years, finding applications as a tool for scientific discovery [1–3]. One such application is the facilitation of quantum experiments by partly or fully automating the experimental work flow in cases where tuning of several parameters is necessary [4,5]. Significant work has already been done toward characterization of multi-quantum-dot devices [6–13] and automated tuning of such systems [14–16]. One common challenge in tuning quantum devices is posed by material imperfections and disorder, which often hinder straightforward navigation through a large parameter space. An important envisioned application of machine learning is thus to characterize or mitigate disorder in quantum devices, yielding optimized device tunings that would be difficult to obtain manually [17–21].

Here, we implement an automated evolutionary strategy for *in situ* optimization of a quantum device. We demonstrate how our tuning protocol can both enhance device functionality and mitigate the effects of disorder. As an illustrative proof of principle, we apply the same optimization algorithm to a numerically simulated device as well as to a real device in experiment, where in both cases we choose the simplest approach resulting in efficient optimization.

We focus on a quantum device for which most of the physics is well understood, namely a quantum point contact (QPC) defined within a GaAs-based two-dimensional electron gas, where the potential landscape in the constriction can be modified via a 3×3 array of electrostatic top gates. The quantized conductance demonstrated in QPCs [22–24] is not only a fundamental hallmark of quantum physics, but has also found important applications in, e.g., quantum sensing of charge [25–32] (an important ingredient in readout of spin qubits [33,34]), interferometry for probing anyonic statistics [35–38], or making switches to toggle between tunneling and ballistic transport [39].

To optimize QPC functionality, i.e., stable plateaus with integer quantized conductance separated by sharp steps, we use a numerical optimization method to make a computer

*These authors contributed equally to this work.

†Contact author: Anasua.Chatterjee@tudelft.nl

‡Contact author: e.p.l.van.nieuwenburg@liacs.leidenuniv.nl

Published by the American Physical Society under the terms of the Creative Commons Attribution 4.0 International license. Further distribution of this work must maintain attribution to the author(s) and the published article's title, journal citation, and DOI.

"learn" how to best engineer the system Hamiltonian. It is useful for the optimizer to be (i) gradient-free; (ii) simple to implement, working well without fine-tuning; and (iii) relatively insensitive to device-specific details influencing the loss landscape for optimization. Several methods satisfy these conditions, including Nelder-Mead, Powell's method, Bayesian optimization, and the covariance matrix adaptation evolution strategy (CMA-ES) [40] algorithm. The former two are deterministic methods, which may not be ideal for highly nonconvex loss landscapes, while the latter two are stochastic methods. We compared these algorithms on our problem (see Supplemental Material [41]), and found that CMA-ES outperforms the others, particularly in situations with disorder. CMA-ES has recently also been identified as a good strategy for tuning proximitized Rashba wires to the topological regime [17,18] or so-called artificial Kitaev chains to sweet spots [21].

Via the nine gate voltages of the 3×3 "pixel-gate" array we have direct control over the potential landscape, and can hence correct for possible microscopic disorder at length scales comparable to the pixel-gate dimensions. We first implement the optimization routine on a simulated device, where we have full control over the properties of the device and disorder, and can experiment with possible functionality metrics. The resulting optimized gate configuration, both with and without random disorder, yields clear quantized conductance plateaus at values consistent with the physics of QPC devices, even as the optimization algorithm remains agnostic about the underlying disorder distribution, and about where the conductance plateaus should occur. More importantly, we then employ the same numerical optimization routine directly on a real device, and also demonstrate *in situ* mitigation of device-specific disorder in an experiment.

Device to optimize—Ballistic electron transport through a QPC occurs in quantized conductance steps of $2e^2/h$, visible in experiments (for sufficient splitting of the energy subbands) as conductance plateaus with sharp jumps between them when the transverse confinement is changed [22,23]. Except in the ideal case at zero temperature, these telltale steps in the quantized conductance curve will to some extent be smoothed out and distorted due to factors such as temperature, scattering off the confining potential itself, or random variations in it due to material disorder [42,43]. Thus constructing a tunable potential landscape to improve the staircase signature of the quantized conductance is of interest.

We consider a 3×3 array of square voltage-controlled gates, analogous to pixels in a camera sensor, patterned between a split-gate structure of two outer gates, see Fig. 1(a). We denote the pixel gate voltages as $V_{\eta\nu}$ (with $\eta, \nu \in \{-1, 0, 1\}$ denoting the pixel position), while the split-gate voltages are named V_{SG1} and V_{SG2}. We will denote the parameter for constricting the QPC transport channel as V_{QPC}, which is the independent variable of the

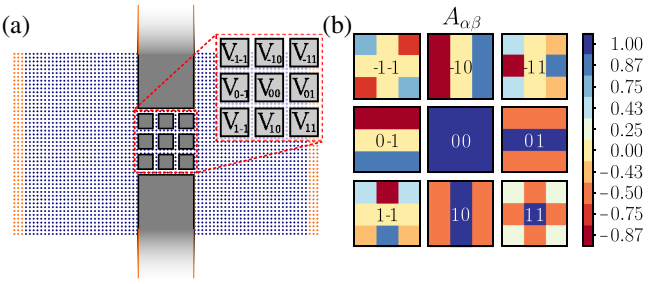

FIG. 1. (a) Cartoon of the gate layout over a tight-binding scattering region. (b) Fourier modes $A_{\alpha\beta}$ of the pixel-gate voltages.

conductance curve. Different choices will result in different behavior; the results of sweeping the outer gates for instance may be of limited quality due to the large distance between them. Other options include keeping the outer gates fixed and sweeping over a pair of pixel-gate voltages in the upper and lower row, such as V_{-10} and V_{10} [see Fig. 1(a)] or sweeping over the average gate voltage of all the pixels. The choice of V_{QPC} has a large impact on the quantized conductance features, since it sets both the effective length and width of the QPC [44]. For now, we will keep the outer gates V_{SG1} and V_{SG2} at fixed values, as they are too far apart to form a QPC on their own and we will not specify V_{QPC} yet. The optimization is done on the pixel gates $V_{\eta\nu}$, either directly on the pixels not used for V_{QPC}, or through the Fourier modes presented in the next section.

We use the CMA-ES algorithm [40], where a population of samples drawn from a multivariate normal distribution (MvN) is ranked according to their "fitness" (defined through a loss function), with a fraction of the fittest samples becoming the basis for the next population. A schematic of the work flow is shown in Fig. 2 (see Supplemental Material for more details [41]).

To quantify how steplike the conductance $G[k]$ looks when sweeping over values of $V_{\mathrm{QPC}}[k]$ (with $k = 1, 2, \ldots, M$ data points), we define a loss function L that favors long regions of small derivatives while penalizing a steadily growing conductance,

$$L = \frac{\sum_{k=1}^{M-1} \sqrt[3]{|G[k+1] - G[k]| + \varepsilon}}{1 + N_{G>\mathrm{thr}}/M}, \tag{1}$$

where the cube root yields a preference of a few large terms over many small terms. A small offset value of $\varepsilon = 0.02(e^2/h)$ is added to reduce the effect of noise, and the term $N_{G>\mathrm{thr}}/M$ in the denominator penalizes closing of the QPC completely, where $N_{G>\mathrm{thr}}$ counts the number of conductance values exceeding a threshold $[2 \times 10^{-5}(e^2/h)]$. We further constrain the allowed range of pixel-gate voltages $V_{\eta\nu}$, and any out-of-bounds voltages are projected to the nearest in-bounds value while getting a penalty proportional to the

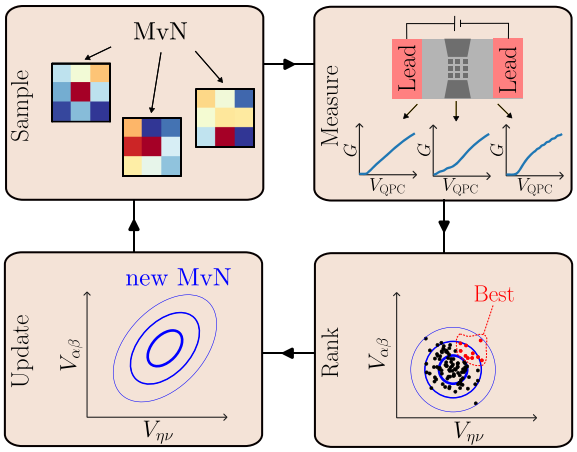

FIG. 2. Schematic of the CMA-ES algorithm interfaced to either a simulation or an actual QPC experiment to optimize the pixel-gate voltages: (i) configurations are sampled, (ii) tested in experiment or simulation, (iii) ranked according to Eq. (1), and (iv) the population is updated.

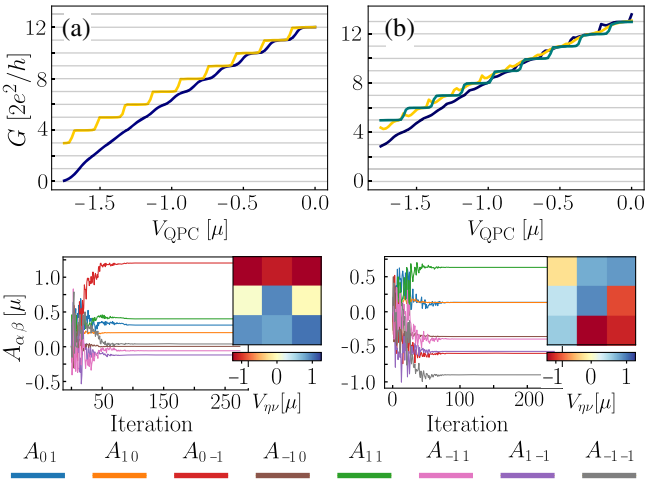

FIG. 3. (a) Conductance for a simulated device without disorder as a function of $V_{QPC} = A_{00}$, with all other Fourier coefficients $A_{\alpha\beta} = 0$ before (blue) and after optimization (yellow). (b) Conductance as a function of V_{QPC} in the presence of disorder characterized by $V_{dis} = 0.352\mu$ and $\lambda_{dis} = 300$ nm. In addition to traces with the same two Fourier coefficient configurations as in (a) (blue, yellow), we show the optimized trace in the presence of the disorder (turquoise). Bottom panels: convergence of the Fourier coefficients (color coding shown at the bottom) during the optimization. Color maps show the final pixel configuration around the average.

square of the distance from the allowed range. Importantly, the loss function does not include any information about the quantized conductance plateau values, i.e., solutions are determined by the physics of quantized conductance rather than any type of "gate-engineered overfitting."

Simulations—We model the 2DEG with gate-defined potentials $E_i(x, y)$ with $i \in \{\mathrm{SG1}, \mathrm{SG2}, (\eta, \nu)\}$ and disorder $E_{dis}(x, y)$ by the continuous Hamiltonian

$$H = -\frac{\hbar^2}{2m^*}(\partial_x^2 + \partial_y^2) - \mu + \sum_i E_i(x, y) + E_{dis}(x, y), \quad (2)$$

where m^* is the effective mass and μ the electrochemical potential. The potentials $E_i(x, y)$ are calculated assuming rectangular gates at a given distance above the 2DEG [45,46], ignoring any dielectric screening in the material. For the disorder potential $E_{dis}(x, y)$ we draw random on-site disorder values $u_{dis}(x, y) \sim \mathrm{uniform}(0, V_{dis})$ and set a correlation length λ_{dis} for the disorder by filtering out short-wavelength modes [17],

$$E_{dis}(x, y) = \mathcal{F}^{-1}\left[e^{-2\pi|\mathbf{q}|\lambda_{dis}}\mathcal{F}[u_{dis}(x, y)]\right], \quad (3)$$

where $f(\mathbf{q}) = \mathcal{F}[f(\mathbf{r})]$ is the Fourier transform of $f(\mathbf{r})$. We discretize the resulting Hamiltonian and simulate the transport properties of our QPC array device using Kwant [47] (see Supplemental Material for details [41]).

Instead of optimizing the pixel voltages $V_{\eta\nu}$ directly, we optimize the Fourier modes $A_{\alpha\beta}$ [shown in panel (b) of Fig. 1], defined by

$$V_{\eta\nu} = \sum_{\alpha,\beta} A_{\alpha\beta} \cos\left(\frac{\pi\alpha}{12}[8\eta - 3(\alpha - 1)]\right) \times \cos\left(\frac{\pi\beta}{12}[8\nu + 3(\beta - 1)]\right), \quad (4)$$

where $\alpha, \beta \in \{-1, 0, 1\}$, and we chose the QPC sweep parameter to be the average pixel voltage $A_{00} = V_{QPC}$. Tuning voltages collectively via Fourier coefficients is more robust than tuning individual gates since we are tuning overall "shapes" of the 2DEG potential rather than individual areas [17]. We can sweep $V_{QPC} = A_{00}$ from -1.75μ to 0, and set the pixel-gate bounds to be $V_{\eta\nu}/\mu \in (-3, 1)$ with $V_{SG1(2)}/\mu = -3$. Here, $n_{pop} = 56$, chosen based on the number of CPU cores.

Simulation results—Optimization was performed for a simulated QPC device both in the absence and presence of disorder. In the top panel of Fig. 3(a) we plot the conductance as a function of the average pixel voltage $V_{QPC} = A_{00}$ for a disorder-free system in the cases of all other Fourier components being either set to zero (blue) or optimized (yellow). Both curves have a steplike shape, with sharper features in the optimized case. The lower panel inset shows the final optimized pixel-gate voltages. Interestingly, the optimized solution is asymmetric [48]. In the top panel of Fig. 3(b) we investigate the case with disorder where $\lambda_{dis} = 300$ nm is comparable to the pixel

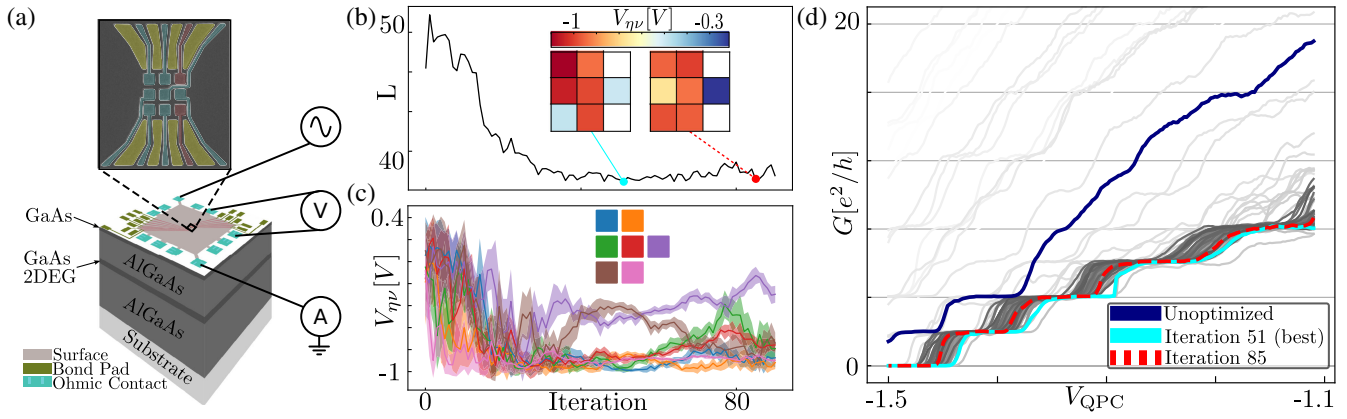

FIG. 4. (a) Device heterostructure and false-colored SEM image, indicating gate functionality in experiment; the yellow outer barriers are all kept at constant voltage offset, red pixel gates are swept from −1.1 to −1.5 V in 200 steps and define the QPC sweeping axis V_{QPC}, and blue pixel gates are optimized by the algorithm. (b) Loss for each iteration of the algorithm, dots are iterations where the best member of the population is shown in (d); the inset shows the optimized voltages for the best member of iteration 51 and 85 (loss values 36.14 and 36.46, respectively). (c) Average voltage for each pixel per iteration, and variance across the population shown in shaded area. Colors correspond to $V_{n\nu}$ according to the inset. (d) Best-scoring member of each iteration, with later iterations appearing darker. The unoptimized result (blue) is the best evaluated staircase in the first iteration of the algorithm, the optimized staircase (light blue) is the best ever seen result (iteration 51), and the dashed red staircase comes from iteration 85.

gate sizes and the magnitude $V_{\mathrm{dis}} = 0.352\mu$ large enough that the staircase for the optimal solution without disorder was visibly degraded after adding the disorder. We show the conductance for a fixed disorder configuration for three different pixel-gate configurations: the two same configurations as in Fig. 3(a) (blue, yellow) and in addition a configuration that was optimized in the presence of disorder (turquoise). The final optimized configuration is again shown in the lower panel inset.

The lower panels in Fig. 3 show the evolution of the eight variables as a function of iteration number during optimization. We see that the algorithm initially probes a relatively large search space but eventually converges toward a voltage configuration that gives a clear conductance staircase. In both cases, the optimization loop was terminated after reaching the maximal time limit of 48 h, rather than converging within the CMA library's default tolerances on change in loss function and optimized parameters [40].

Already without disorder, an optimized potential landscape has more pronounced steps than when only the average pixel values are swept. It appears that the visibility of plateaus in the unoptimized case lowers as the channel becomes more constrained, possibly due to differences in how much the potential shape is changed along the x and y directions as the pixel-gate voltages are swept. In the presence of disorder, the staircase that had vanished due to it reappears after tuning the gates to new values, indicating that it can adapt to a certain extent to the randomness.

Although the optimized disordered devices nearly always outperform those configured for no disorder or without any optimization at all (see Supplemental Material [41]), there are occurrences where the disorder potential and the disorder-free solution for the pixel voltages together form a potential that results in a decent staircase. Lastly, all plateaus occurring on integer conductance values without having coded this as a constraint into the loss function indicates that the solution is indeed a manifestation of QPC physics.

Experimental setup—Finally, we turn to the experimental application of our technique on a device consisting of a pixelated QPC, similar to the simulated design, fabricated on a GaAs heterostructure. The device used is shown in Fig. 4(a), with fabrication and experimental setup described in Supplemental Material [41]. The CMA-ES capabilities demonstrated in the simulation were implemented on this device live, without human intervention. The exact tuning protocol was modified slightly to run smoothly on a real device with fabrication constraints stemming from the need to route the pixelated gates and make contact to them, which inherently breaks the device symmetry. Primarily (see Supplemental Material for full details [41]), the rectangular outer gates were split into eight tapered gates held at the same voltage, and the spacing between pixels was made sufficiently large to accommodate the thin routing lines. As this breaks the symmetry necessary for Fourier-mode tuning, we now consider individual pixel-gate voltages $\mathrm{V_{ij}}$ instead. We apply V_{QPC} to two opposing pixels [colored red in Fig. 4(a)], i.e., $V_{\mathrm{QPC}} = V_{-11} = V_{11}$, and let the algorithm freely optimize all other seven pixel voltages.

Experimental results—The algorithm autonomously optimized from a starting point of 0 V for all pixel gates not used as V_{QPC}. Each pixel was bounded to $[-1.5\ \mathrm{V}, 0.3\ \mathrm{V}]$ to prevent device damage and hysteresis effects. The algorithm generally converged to regions with

lower loss values than it started with. An example run is shown in Fig. 4(b), where it drops gradually for the first 30 iterations, and then remains steady. The inset shows examples of two of the best voltage configurations, runs 51 and 85.

We note the voltages keep drifting considerably after iteration 51 (the best solution) until the end of the optimization. This effect is even clearer from Fig. 4(c), where pixel-gate averages and variances for each iteration are plotted, showing that even toward the end of the run the algorithm is still exploring. There are several explanations for this behavior, including heating effects from measuring for extended periods during the run and flat plateaus in the loss landscape where multiple configurations are equally good [49]. A likely explanation is measurement noise, which can turn the latest iterations of the optimization into an effective random walk; this occurs when the losses of individual members get so close to each other that the ranking used by the algorithm is in fact determined by measurement noise.

In Fig. 4(d) we show the results of the run in terms of the QPC traces obtained. The unoptimized trace (blue) is the lowest loss (best) member of the first iteration of the algorithm, showing no steplike conductance features. The final optimized version (light blue) is the best member of all iterations, here from iteration 51, where steplike features are clearly visible. We attribute this to the formation of a ballistic transport constriction, indicating a successful tuning of the QPC. A promising member (dashed red) from iteration 85 is also shown; interestingly it also appears with well defined conductance plateaus even though the pixel voltages are quite different from iteration 51 [see inset of panel (b) in Fig. 4]. Each iteration has a population of nine members, meaning that the optimization found an optimum within 460 total measurements, which takes ∼9 h in our setup.

The two configurations exemplified in Fig. 4(d) (iterations 51 and 85) show excellent step behavior in their $G(V_{\mathrm{QPC}})$ traces, yet their pixel configurations [insets of Fig. 4(b)] indicate a significantly different landscape. This may indicate that the optimized voltages found by the algorithm are not concomitant to one QPC model potential, such as the canonical saddle-point potential. This could be due to device asymmetry and how the routing to the pixel gates influences the potential in the 2DEG. It could also mean that the algorithm optimizes pixel-gate potentials to mitigate disorder potentials in the heterostructure or device, rather than defining a particular potential; this would be an important point for tuning of semiconductor quantum devices in general. For the particular case of QPC tuning, this could be alleviated by further measurements and improved device design, preferably low-impurity heterostructures.

Conclusions and outlook—The results show that automated tuning of a QPC device with a 3×3 array of tunable electrostatic gates using the CMA-ES algorithm gives more pronounced quantized conductance steps by optimizing the shape of the potential in the conductance channel. Through simulations we found that the algorithm is capable of adapting to random disorder on length scales comparable to the tunable gates. We furthermore demonstrated the CMA-ES algorithm on a real device, showing how it improved the conductance curves *in situ*. Although the actual experiment was limited to only tuning seven out of nine pixel gates, an improved device design featuring a multilayer gate structure could possibly fix this issue in the future. Another outlook for future projects could be to allow voltage configurations that vary as a function of the sweeping parameter V_{QPC}, for instance by writing the Fourier coefficients $A_{\alpha\beta} = A_{\alpha\beta}(V_{\mathrm{QPC}})$ as low-order polynomials where the prefactors can be tuned.

Acknowledgments—We acknowledge fruitful discussions with and contributions from A. R. Akhmerov. We also thank Xavier Waintal and Bernd Rosenow for initial discussions on this work and related projects. This project was funded within the QuantERA II Programme that has received funding from the European Union's Horizon 2020 research and innovation programme under Grant Agreement No. 101017733. It is part of INTFELLES-Project No. 333990, which is funded by the Research Council of Norway (RCN), and it received funding from the Dutch National Growth Fund (NGF) as part of the Quantum Delta NL programme. Simulations were performed on resources provided by the NTNU IDUN/EPIC computing cluster [50]. A. C. and T. R. acknowledge support from the Inge Lehmann Programme of the Independent Research Fund Denmark, and the U.S. Army Research Office (ARO) under Award No. W911NF-24-2-0043. J. B. acknowledges additional support from RCN through its Centers of Excellence funding scheme, Project No. 262633, "QuSpin". C. M. M. acknowledges a research grant (Project No. 43951) from VILLUM FONDEN. O. K. received funding via the Innovation Fund Denmark for the project DIREC (9142-00001B).

Data availability—The data that support the findings of this article are openly available [51,52].

[1] T. Neupert, M. H. Fischer, E. Greplova, K. Choo, and M. M. Denner, *Machine Learning Kompakt* (Springer Spektrum, Wiesbaden, 2022), 10.1007/978-3-658-32268-7.

[2] A. Dawid *et al.*, Modern applications of machine learning in quantum sciences, arXiv:2204.04198.

[3] V. Gebhart, R. Santagati, A. A. Gentile, E. M. Gauger, D. Craig, N. Ares, L. Banchi, F. Marquardt, L. Pezze', and C. Bonato, Learning quantum systems, Nat. Rev. Phys. **5**, 141 (2023).

[4] N. Ares, Machine learning as an enabler of qubit scalability, Nat. Rev. Mater. **6**, 870 (2021).
[5] J. P. Zwolak and J. M. Taylor, Colloquium: Advances in automation of quantum dot devices control, Rev. Mod. Phys. **95**, 011006 (2023).
[6] V. Nguyen, S. B. Orbell, D. T. Lennon, H. Moon, F. Vigneau, L. C. Camenzind, L. Yu, D. M. Zumbühl, G. A. D. Briggs, M. A. Osborne, D. Sejdinovic, and N. Ares, Deep reinforcement learning for efficient measurement of quantum devices, npj Quantum Inf. **7**, 100 (2021).
[7] A. Zubchenko, D. Middlebrooks, T. Rasmussen, L. Lausen, F. Kuemmeth, A. Chatterjee, and J. P. Zwolak, Autonomous bootstrapping of quantum dot devices, Phys. Rev. Appl. **23**, 014072 (2025).
[8] S. S. Kalantre, J. P. Zwolak, S. Ragole, X. Wu, N. M. Zimmerman, M. D. Stewart, and J. M. Taylor, Machine learning techniques for state recognition and auto-tuning in quantum dots, npj Quantum Inf. **5**, 6 (2019).
[9] O. Krause, A. Chatterjee, F. Kuemmeth, and E. van Nieuwenburg, Learning Coulomb diamonds in large quantum dot arrays, SciPost Phys. **13**, 084 (2022).
[10] O. Krause, B. Brovang, T. Rasmussen, A. Chatterjee, and F. Kuemmeth, Estimation of convex polytopes for automatic discovery of charge state transitions in quantum dot arrays, Electronics **11**, 2327 (2022).
[11] R. Koch, D. Van Driel, A. Bordin, J. L. Lado, and E. Greplova, Adversarial Hamiltonian learning of quantum dots in a minimal Kitaev chain, Phys. Rev. Appl. **20**, 044081 (2023).
[12] J. R. Taylor and S. Das Sarma, Neural network based deep learning analysis of semiconductor quantum dot qubits for automated control, Phys. Rev. B **111**, 035301 (2025).
[13] D. van Driel *et al.*, Cross-platform autonomous control of minimal Kitaev chains, arXiv:2405.04596.
[14] H. Moon, D. T. Lennon, J. Kirkpatrick, N. M. van Esbroeck, L. C. Camenzind, L. Yu, F. Vigneau, D. M. Zumbühl, G. A. D. Briggs, M. A. Osborne, D. Sejdinovic, E. A. Laird, and N. Ares, Machine learning enables completely automatic tuning of a quantum device faster than human experts, Nat. Commun. **11**, 4161 (2020).
[15] R. Durrer, B. Kratochwil, J. V. Koski, A. J. Landig, C. Reichl, W. Wegscheider, T. Ihn, and E. Greplova, Automated tuning of double quantum dots into specific charge states using neural networks, Phys. Rev. Appl. **13**, 054019 (2020).
[16] J. Ziegler, F. Luthi, M. Ramsey, F. Borjans, G. Zheng, and J. P. Zwolak, Tuning arrays with rays: Physics-informed tuning of quantum dot charge states, Phys. Rev. Appl. **20**, 034067 (2023).
[17] M. Thamm and B. Rosenow, Machine learning optimization of Majorana hybrid nanowires, Phys. Rev. Lett. **130**, 116202 (2023).
[18] M. Thamm and B. Rosenow, Conductance based machine learning of optimal gate voltages for disordered Majorana wires, Phys. Rev. B **109**, 045132 (2024).
[19] D. L. Craig, H. Moon, F. Fedele, D. T. Lennon, B. Van Straaten, F. Vigneau, L. C. Camenzind, D. M. Zumbühl, G. A. D. Briggs, M. A. Osborne, D. Sejdinovic, and N. Ares, Bridging the reality gap in quantum devices with physics-aware machine learning, Phys. Rev. X **14**, 011001 (2024).
[20] E. Chatzikyriakou, J. Wang, L. Mazzella, A. Lacerda-Santos, M. Cecilia da Silva Figueira, A. Trellakis, S. Birner, T. Grange, C. Bäuerle, and X. Waintal, Unveiling the charge distribution of a GaAs-based nanoelectronic device: A large experimental dataset approach, Phys. Rev. Res. **4**, 043163 (2022).
[21] J. Benestad, A. Tsintzis, R. S. Souto, M. Leijnse, E. van Nieuwenburg, and J. Danon, Machine-learned tuning of artificial Kitaev chains from tunneling spectroscopy measurements, Phys. Rev. B **110**, 075402 (2024).
[22] D. A. Wharam, T. J. Thornton, R. Newbury, M. Pepper, H. Ahmed, J. E. F. Frost, D. G. Hasko, D. C. Peacock, D. A. Ritchie, and G. A. C. Jones, One-dimensional transport and the quantisation of the ballistic resistance, J. Phys. C **21**, L209 (1988).
[23] B. J. van Wees, H. van Houten, C. W. J. Beenakker, J. G. Williamson, L. P. Kouwenhoven, D. van der Marel, and C. T. Foxon, Quantized conductance of point contacts in a two-dimensional electron gas, Phys. Rev. Lett. **60**, 848 (1988).
[24] M. Büttiker, Quantized transmission of a saddle-point constriction, Phys. Rev. B **41**, 7906(R) (1990).
[25] M. Field, C. G. Smith, M. Pepper, D. A. Ritchie, J. E. F. Frost, G. A. C. Jones, and D. G. Hasko, Measurements of Coulomb blockade with a noninvasive voltage probe, Phys. Rev. Lett. **70**, 1311 (1993).
[26] J. M. Elzerman, R. Hanson, L. H. Willems van Beveren, B. Witkamp, L. M. K. Vandersypen, and L. P. Kouwenhoven, Single-shot read-out of an individual electron spin in a quantum dot, Nature (London) **430**, 431 (2004).
[27] J. R. Petta, A. C. Johnson, J. M. Taylor, E. A. Laird, A. Yacoby, M. D. Lukin, C. M. Marcus, M. P. Hanson, and A. C. Gossard, Coherent manipulation of coupled electron spins in semiconductor quantum dots, Science **309**, 2180 (2005).
[28] D. J. Reilly, C. M. Marcus, M. P. Hanson, and A. C. Gossard, Fast single-charge sensing with a rf quantum point contact, Appl. Phys. Lett. **91**, 162101 (2007).
[29] M. C. Cassidy, A. S. Dzurak, R. G. Clark, K. D. Petersson, I. Farrer, D. A. Ritchie, and C. G. Smith, Single shot charge detection using a radio-frequency quantum point contact, Appl. Phys. Lett. **91**, 222104 (2007).
[30] S. Gustavsson, R. Leturcq, M. Studer, I. Shorubalko, T. Ihn, K. Ensslin, D. C. Driscoll, and A. C. Gossard, Electron counting in quantum dots, Surf. Sci. Rep. **64**, 191 (2009).
[31] C. Barthel, D. J. Reilly, C. M. Marcus, M. P. Hanson, and A. C. Gossard, Rapid single-shot measurement of a singlet-triplet qubit, Phys. Rev. Lett. **103**, 160503 (2009).
[32] C. Bäuerle, D. C. Glattli, T. Meunier, F. Portier, P. Roche, P. Roulleau, S. Takada, and X. Waintal, Coherent control of single electrons: A review of current progress, Rep. Prog. Phys. **81**, 056503 (2018).
[33] L. M. K. Vandersypen, H. Bluhm, J. S. Clarke, A. S. Dzurak, R. Ishihara, A. Morello, D. J. Reilly, L. R. Schreiber, and M. Veldhorst, Interfacing spin qubits in quantum dots and donors—hot, dense, and coherent, npj Quantum Inf. **3**, 34 (2017).
[34] G. Burkard, T. D. Ladd, A. Pan, J. M. Nichol, and J. R. Petta, Semiconductor spin qubits, Rev. Mod. Phys. **95**, 025003 (2023).
[35] W. Bishara, P. Bonderson, C. Nayak, K. Shtengel, and J. K. Slingerland, Interferometric signature of non-Abelian anyons, Phys. Rev. B **80**, 155303 (2009).

[36] B. Rosenow, I. P. Levkivskyi, and B. I. Halperin, Current correlations from a mesoscopic anyon collider, Phys. Rev. Lett. **116**, 156802 (2016).
[37] H. Bartolomei, M. Kumar, R. Bisognin, A. Marguerite, J.-M. Berroir, E. Bocquillon, B. Plaçais, A. Cavanna, Q. Dong, U. Gennser, Y. Jin, and G. Fève, Fractional statistics in anyon collisions, Science **368**, 173 (2020).
[38] J. Nakamura, S. Liang, G. C. Gardner, and M. J. Manfra, Fabry-Pérot interferometry at the $\nu = 2/5$ fractional quantum Hall state, Phys. Rev. X **13**, 041012 (2023).
[39] D. P. E. Smith, Quantum point contact switches, Science **269**, 371 (1995).
[40] N. Hansen, The CMA evolution strategy: A tutorial, arXiv:1604.00772.
[41] See Supplemental Material at http://link.aps.org/supplemental/10.1103/13c4-p4fq for additional details about simulations, experimental setup, and device fabrication.
[42] Thomas Ihn, *Semiconductor Nanostructures: Quantum States and Electronic Transport* (Oxford University Press, Oxford, 2010).
[43] For a wider QPC the energy differences between levels shrink, increasing the impact of such smoothening processes.
[44] M. J. Iqbal, R. Levy, E. J. Koop, J. B. Dekker, J. P. de Jong, J. H. M. van der Velde, D. Reuter, A. D. Wieck, R. Aguado, Y. Meir, and C. H. van der Wal, Odd and even Kondo effects from emergent localization in quantum point contacts, Nature (London) **501**, 79 (2013).
[45] J. H. Davies, I. A. Larkin, and E. V. Sukhorukov, Modeling the patterned two-dimensional electron gas: Electrostatics, J. Appl. Phys. **77**, 4504 (1995).
[46] N. L. Foulk and S. Das Sarma, Theory of charge stability diagrams in coupled quantum dot qubits, arXiv:2409.02301.
[47] C. W. Groth, M. Wimmer, A. R. Akhmerov, and X. Waintal, Kwant: A software package for quantum transport, New J. Phys. **16**, 063065 (2014).
[48] Additional optimization runs show that the algorithm also finds the mirror image solution; see Supplemental Material [41].
[49] Ill-behaved gate hysteresis may also prevent convergence of the algorithm. To minimize this when measuring traces as in Fig. 4(d), we hold the device at the initial gate voltages for at least 10 s before sweeping V_{QPC}.
[50] M. Själander, M. Jahre, G. Tufte, and N. Reissmann, EPIC: An energy-efficient, high-performance GPGPU computing research infrastructure, arXiv:1912.05848.
[51] https://github.com/jacobdben/qpcRL/tree/main.
[52] T. Rasmussen, J. Benestad, B. Brovang, O. Krause, J. Danon, F. Kuemmeth, A. Chatterjee, and E. van Nieuwenburg, qpcRL, 2024, 10.5281/zenodo.17404486.